Composites Part B 193 (2020) 107987

Contents lists available at ScienceDirect

Composites Part B

journal homepage: www.elsevier.com/locate/compositesb

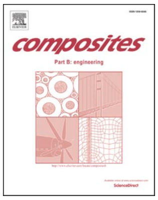

High performance epoxy composites prepared using recycled short carbon fiber with enhanced dispersibility and interfacial bonding through polydopamine surface-modification

Xianhua Huan [a], Ke Shi [a], Jiqiang Yan [a], Song Lin [c], Yanjie Li [a], Xiaolong Jia [a,b,*], Xiaoping Yang [a,b]

[a] State Key Laboratory of Organic-Inorganic Composites, College of Materials Science and Engineering, Beijing University of Chemical Technology, Beijing, 100029, PR China
[b] Key Laboratory of Carbon Fiber and Functional Polymer, Ministry of Education, Beijing University of Chemical Technology, Beijing, 100029, PR China
[c] North China Institute of Aerospace Engineering, Hebei, 065000, PR China

ARTICLE INFO

Keywords:
Polymer-matrix composites (PMCs)
Recycling
Interface/interphase
Surface treatments

ABSTRACT

The critical issue and challenge in reusing recycled carbon fiber (rCF) was to fully exerting its outstanding properties via an efficient and environmental-friendly way. In this study, the strengthening effects of polydopamine surface-modified recycled short CF (pDop-rSCF) on mechanical, thermo-mechanical, electrical and electromagnetic properties of epoxy (EP)-based composites were systematically evaluated. The dispersibility of pDop-rSCF in suspension used for fabricating nonwoven mat was quantitatively characterized with crowding factor N, dispersion coefficient β and fractal dimension D. Significant enhancements were achieved in tensile and flexural properties, interlaminar shear strength, storage modulus and electromagnetic interference shielding capability of EP composites reinforced with pDop-rSCF nonwoven mat, which was primarily ascribed to chemically strengthened interfacial bonding between pDop-rSCF and EP matrix and the increased connectivity among pDop-rSCFs with excellent dispersion.

1. Introduction

Carbon fiber reinforced polymers (CFRP) have been widely used in various industrial fields, due to their outstanding properties of high strength/stiffness-to-weight ratio, low density, good corrosion resistance and easy processability, etc [1–5]. In recent years, demands for CFRP grew very fast in aerospace and wind electricity applications for light weighting and in automotive industries for attaining greater fuel efficiency and lower greenhouse gas emission [2,5], while raising concerns about environmental pollution. Inevitably, such concerns caused by CFRP wastes were hot topic in both academic and industrial community, which promoted the environmental legislation on how to manage the CFRP wastes in a green and environmental-friendly solution in many countries [5–7]. Given high cost and massive energy consumption in production of CF, the reuse of recycled CF (rCF) was extensively believed as the most promising and sustainable approach [4,8]. Thus, various types of techniques were developed to recover CF from CFRP wastes, such as mechanical processes (mainly grinding) [9], thermal pyrolysis [6,9,10], superheated steam treatment [11] and solvolysis [11,12], etc. Among these reported techniques, the pyrolysis was the most mature and feasible one, which has been commercially exploited and reached an industrial scale [6,9,10]. In our previous work, a catalytic pyrolysis technology was explored to reclaim high-quality rCF from epoxy (EP) resin, based on efficient solubility and catalytic activity of molten $ZnCl_2$ [13].

Noticeably, rCF could be called a type of “new material”, since it was much different from freshly produced CF in the aspects of morphology and surface characteristics [4,8]. rCF was often discontinuous in a form of short fiber with wide length distribution as CFRP wastes required to be cut into smaller pieces before thermal pyrolysis. More differently, rCF lost the sized layer during the thermal recovering, while fresh CF was sized by polymeric components. As a result, rCF generally existed in a state of short fiber bundles. Naturally, it met lots of difficulties in reusing rCF in different fields, especially as the reinforcement in the

---

[*] Corresponding author. State Key Laboratory of Organic-Inorganic Composites, College of Materials Science and Engineering, Beijing University of Chemical Technology, Beijing, 100029, PR China.

E-mail address: jiaxl@mail.buct.edu.cn (X. Jia).

https://doi.org/10.1016/j.compositesb.2020.107987
Received 31 October 2019; Received in revised form 17 March 2020; Accepted 18 March 2020

polymer-based composites, because the obvious changes in morphology and surface characteristics greatly limited the performance efficiency of rCF due to the bad dispersion and poor interfacial bonding in the polymer matrix or in other mediums [14–16]. Therefore, in preparing rCF reinforced polymer composites, the main challenges focused on how to control the dispersion state of rCF easily and achieve good interfacial bonding in the matrix effectively.

A large number of scientific works have reported that surface modification was an effective technical strategy to enhance the dispersibility and interfacial bonding of fiber-type fillers in polymer composites, including chemical oxidation [17], plasma processing [15,18], electrochemical treatment [19], surface grafting [20], and physical adsorption [21,22], etc. However, it should be mentioned that the surface modification in reported methods like chemical oxidation would hurt the bulk strength of CF with using abundant amounts of oxidant chemicals and organic solvents. And the embarrassing problem was that such surface modification increased the cost of rCF close to or even higher than that of as-produced CF. Actually, it was strongly expected to solve the above difficulties through a relatively environmental-friendly and low-cost approach, since the reusing process of rCF should not generate pollution again and at best was carried out in a cheap routine with high recycling efficiency. Luckily, the efficient surface grafting by using mussel-inspired modifiers such as dopamine was probably an effective and environmental-friendly way to enhance the interfacial bonding between filler and polymer matrix through possible interfacial reactions [23–25], which also positively affected the dispersibility of filler in polymer matrix or in other mediums [26,27]. In comparison with the synthetic binders, the bio-based binder dopamine showed the outstanding advantages of good water-solubility, superior adhesion to any substrates through the reactive groups (such as amino and catechol groups), mild reaction condition for practical application and low cost [23–27]. As reported in some publications [22,24,27] and our previous works [26,28], the dopamine modification on carbon-based fillers like GO much contributed to the enhancement in overall properties of polymer composites. Thus, it was definitely meaningful to evaluate and verify the above-mentioned advantages of dopamine in reusing rCF to prepare the high performance of polymer composites.

Hence, in this study, mussel-inspired polydopamine was used as the active modifier for surface modification on recycled short CF (rSCF). Initially, polydopamine surface-modified rSCF (pDop-rSCF) was readily prepared via the mild oxidative polymerization of dopamine in a weak alkaline condition ($pH = 8.5$). The surface characteristics of pDop-rSCF were systematically characterized with Fourier transform infra-red spectroscope (FT-IR), X-ray photoelectron spectroscope (XPS), thermogravimetric analysis (TGA), scanning electron microscope (SEM) and atomic-force microscope (AFM), etc. Then, the dispersion state of pDop-rSCF in the environmental-friendly medium water and the structural uniformity of pDop-rSCF nonwoven mat prepared with pDop-rSCF suspension were investigated, along with discussing the dispersion mechanism of pDop-rSCF in water. Afterwards, pDop-rSCF nonwoven mat was applied as the reinforcement to fabricate pDop-rSCF/EP composites, and the corresponding rSCF/EP composites were used as comparisons. The strengthening effect of pDop-rSCF on EP composites was comprehensively investigated by testing tensile and flexural properties, representative stress-strain curves with cumulative acoustic emission (AE) energy, as well as interlaminar shear strength (ILSS) and thermomechanical properties. Moreover, the strengthening effect of pDop-rSCF was further evaluated by measuring electrical conductivity and electromagnetic interference (EMI) shielding properties of pDop-rSCF/EP composites. Aiming to understand the enhancements in interfacial bonding and EMI performance of pDop-rSCF/EP composites, the reasonable mechanisms were proposed and discussed.

2. Experimental section

2.1. *Materials*

rCFs (PAN-based T800H, Toray, Japan) with the diameter of 5 μm were made from abandoned CF/EP composites through catalytic pyrolysis in molten $ZnCl_2$ as reported in our previous work [13]. Dopamine hydrochloride was purchased from Sigma and used directly for the surface modification. The resin matrix, triglycidyl-p-aminophenol (TGPAP) type EP resin (EP value, 0.9), was supplied by Shell Co. The diluter, tetrahydrophthalic acid diglycidyl ester (EP value, 0.65–0.75) was synthesized by authors to reduce the viscosity of TGPAP resin. The hardener, DETDA (composed of 74–80 wt% 3,5-diethyltoluene-2, 4-diamine and 20–26 wt% 3,5-diethyltoluene-2,6-diamine, Ahew 44.3), was obtained from Lonza (Switzerland). All other chemicals and reagents were purchased from Beijing Chemical Works (China) and used directly.

2.2. *Preparation and characterization of pDop-rSCF*

rCF was chopped into ~4 mm in length to prepare the rSCF. Referring to our previous work [26], the schematic preparation of pDop-rSCF is shown in Fig. 1a. Briefly, 1 g rSCF was immersed into 2000 ml H_2O and then treated by 800 W ultra-sonication for 30 min, followed by the addition of 0.1 g dopamine. The pH of the solution was adjusted to be 8.5 by Tris-buffer solution. And the whole mixture system was continuously treated by 800 W ultra-sonication and mechanical agitation at 25 °C for 24 h in an ice water bath. To avoid overheating during this process, the ultrasonication was conducted for 30 min working at intervals of 5 min. After the reaction, the product was centrifuged, washed with deionized water several times and dried in vacuum oven for 24 h at 40 °C to yield pDop-rSCF.

Chemical structures of rSCF and pDop-rSCF were detected with Fourier transform infra-red spectroscope (FT-IR, Nexus670, Nicolet). Element analysis on rSCF and pDop-rSCF was conducted on X-ray photoelectron spectroscope (XPS, ESCALAB 250, Thermo Scientific) using monochromatized Al Ka X-ray source at a constant analyzer. Thermogravimetric analysis (TGA, Q800, TA) was carried out at a heating rate of 10 °C/min from 25 to 700 °C under nitrogen atmosphere. All morphological observations were performed on scanning electron microscope (SEM, S4700, Hitachi). Before SEM examination, specimens were coated with a thin layer of a gold alloy. Diameters of rSCF and pDop-rSCF were averages of ten measurements based on SEM images. Typical tapping-mode atomic-force microscope (AFM, Solver P47H, NT-MDT) measurements were performed using Dimension FastScan from Bruker. Surface wettability of rSCF and pDop-rSCF was characterized by optical contact angle measuring device (OCA20, Dataphysics). Dynamic contact angle between fiber and liquid was measured using dynamic contact angle meter (DCAT21, Dataphysics). The surface energy (γ_f), including dispersive (γ_f^d) and polar (γ_f^p) components, was calculated using the following equations (1) and (2):

$$\gamma_l(1+cos\theta)=2\left(\gamma_l^p\gamma_f^p\right)^{1/2}+2\left(\gamma_l^d\gamma_f^d\right)^{1/2} \tag{1}$$

$$\gamma_f=\gamma_f^p+\gamma_f^d \tag{2}$$

where γ_l, γ_l^p, γ_l^d are the total, polar and dispersive surface energy of liquid, γ_f, γ_f^p , γ_f^d are the total, polar and dispersive surface energy of fiber, and θ denotes the dynamic contact angle between fiber and liquid. For deionized water, $\gamma_l^d = 21.8$ mN/m and $\gamma_l^p = 51.0$ mN/m. For diiodomethane, $\gamma_l^d = 50.8$ mN/m and $\gamma_l^p = 0$ mN/m.

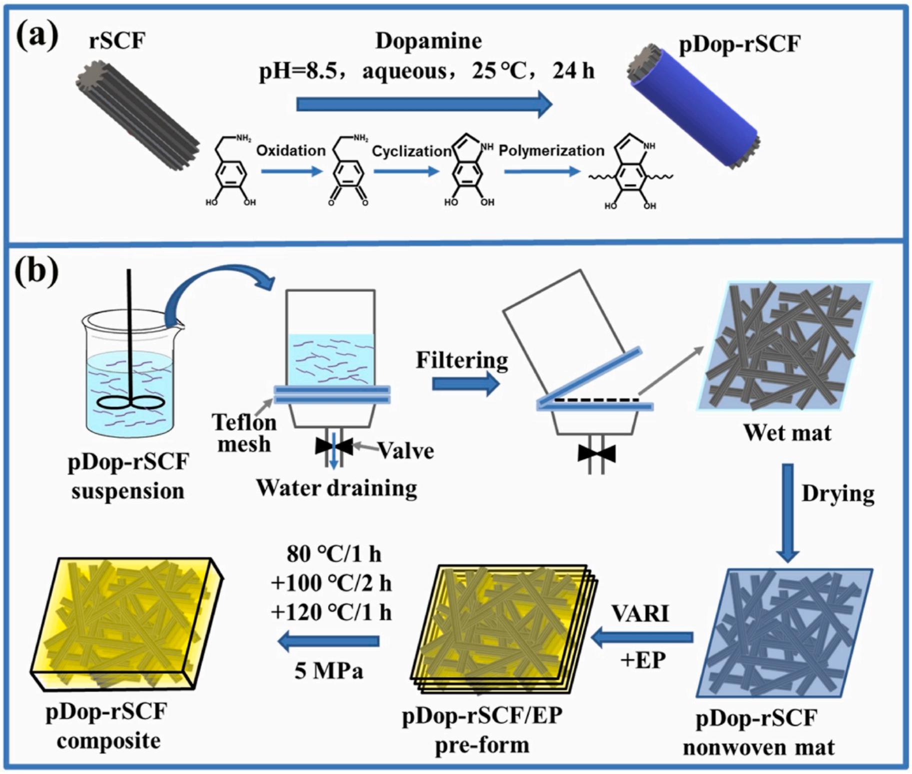

Fig. 1. Schematic showing the preparation of (a) pDop-rSCF and (b) pDop-rSCF nonwoven mat and pDop-rSCF/EP composites.

2.3. Preparation and characterization of pDop-rSCF suspension and pDop-rSCF nonwoven mat

The schematic preparation of pDop-rSCF suspension and pDop-rSCF nonwoven mat is shown in Fig. 1b pDop-rSCF was dispersed into 1000 ml water under stirring and then treated by 800 W ultra-sonication for 30 min in an ice water bath, with the concentration of fiber in water being adjusted to be in the range of 0–25 g/L. To avoid overheating during this process, the ultrasonication was conducted for 8 min working at intervals of 2 min. The above pDop-rSCF suspension was used to prepare nonwoven mat by a similar method to papermaking process [29–31]. The resultant suspension was poured into a filtration unit, and the pDop-rSCF was gradually filtered out of the suspension by draining the water through Teflon mesh belt under vacuum. Finally, the pDop-rSCF nonwoven mat was obtained after the wet mat was dried to remove the water residue completely. For comparison, rSCF suspension and rSCF nonwoven mat were prepared at the same condition. The areal densities of both pDop-rSCF and rSCF nonwoven mats were controlled to be $\sim 20.0 \pm 0.1\ \mathrm{g/m^2}$.

The crowding factor N, which was defined as the number of fibers in a spherical volume of diameter equal to the length of a fiber, was used to direct the preparation of well-dispersed fiber suspension. It was helpful in determining the optimum fiber concentration and could reflect the influence of fiber concentration on dispersion state [32]. Values for N could be calculated using Equation (3):

$$\mathrm{N} = \frac{2}{3} C_V \left(\frac{L}{d}\right)^2 \tag{3}$$

where C_V is volumetric concentration of fibers, L is fiber length and d is fiber diameter. For fiber suspensions, it was often convenient to use mass concentration and fiber coarseness to calculate N. As a result, Equation (3) could be further expressed as Equation (4):

$$\mathrm{N} \approx \frac{5 C_m L^2}{\omega} \tag{4}$$

where C_m is mass concentration of fibers, L is fiber length and ω is fiber coarseness. The dispersion coefficient β was applied to characterize the macro-scale dispersion of rSCF or pDop-rSCF in water. Ten samples were taken out from rSCF or pDop-rSCF suspension randomly and the volume of each sample was 10 ml β value could be calculated using the following Equations (5)–(7):

$$\mathrm{S(x)} = \sqrt{\frac{\sum_{i=1}^{n} (x_i - \overline{x})^2}{n-1}} \tag{5}$$

$$\phi(\mathrm{x}) = \frac{S(x)}{\overline{x}} \tag{6}$$

$$\beta = e^{-\phi(x)} \tag{7}$$

where, x_i is the fiber weight of each sample, $\overline{x}$ is the mean value of fiber weight of n samples, n is the numbers of samples (n is 10 in this study), $S(x)$ is standard deviation, $\phi(x)$ is the variation coefficient and β is the dispersion coefficient. The closer that the β value was to 1, the better the rSCF dispersion was.

To characterize the micro-scale dispersion of rSCF or pDop-rSCF in water, box counting method based on fractal analysis was introduced [33–36]. The fractal dimension (D) of an image indicated the degree of self-similarity and space filling, which reflected the dispersion coefficient effectively. The software, ImageJ, was used to evaluate the fractal dimension of rSCF or pDop-rSCF via the box counting method. Firstly, two-dimensional (2D) optical images of rSCF or pDop-rSCF suspension were captured on optical microscope (OM, CK41, OLYMPUS) and converted into binary images (black: fibers, white: background). Then, ImageJ was applied to find the edges of black patterns and obtain the border images. Afterwards, the FracLac plug-in for ImageJ software was applied to divide border image into small squares (boxes) with same area size, and the number of boxes containing parameters of pattern edges ($\mathrm{N}(r_i)$) and the size of per box(r_i) was recorded. The relationship between $\mathrm{N}(r_i)$ and r_i could be expressed by Equation (8):

$$\mathrm{N}(r_i) \propto \left(\frac{1}{r_i}\right)^D \tag{8}$$

By plotting $\mathrm{Ln}(\mathrm{N}(r_i))$ versus $\mathrm{Ln}(\frac{1}{r_i})$, the value of fractal dimension D could be obtained from the slope of the curve. In our analysis, the side length of box ranged from 5 to 101 pixels in a 1944 × 1944 pixel image, which meant that the size of box ranged from 0.0026 to 0.0478 as the size of whole image was determined to be 1.

2.4. Preparation and characterization of pDop-rSCF/EP composites

The schematic preparation of pDop-rSCF/EP composites is also shown in Fig. 1b. Firstly, EP mixture was obtained by mixing EP resin, DETDA, diluter at the feeding ratios of 70 : 30: 30. Then, the technology of vacuum assisted resin injection (VARI) was utilized to assist the EP mixture to penetrate into the pDop-rSCF nonwoven mat and then the produced pre-form was placed in a semi-closed mold. The curing process of the pre-form was carried out at 80 °C for 1 h, 100 °C for 2 h and 120 °C for 1 h under the pressure of 5 MPa. The weight content of pDop-rSCF in final composites was determined to be ~30 wt% by controlling the feeding ratio of pDop-rSCF nonwoven mat and EP resin. For comparison, rSCF/EP composites were prepared under the same processing condition. The pristine EP was also prepared by pouring EP mixtures into molds and curing at 80 °C for 1 h, 100 °C for 2 h and 120 °C for 1 h as described in our previous works [28,37].

Fractured surfaces of both rSCF/EP and pDop-rSCF/EP composites were observed by SEM (S4700, Hitachi). Tensile and flexural properties as well as interlaminar shear strength (ILSS) of both rSCF/EP and pDop-rSCF/EP composites were measured by mechanical testing machine (INSTRON 1121) according to ASTM D 3039, ASTM D 7264, and ASTM D 2344, respectively. All final values of mechanical properties were averages of five measurements. Crack propagations in both rSCF/EP and pDop-rSCF/EP composites were measured with AE analyzer (SAEU3H, Beijing Shenghua) equipped with 2 sensors at an operating frequency range of 60–400 kHz as described in our previous works [38,39]. The AE signals were detected based on triggering using 50/150/1000 μs□as Peak-Definition-Time/Hit-Definition-Time/Hit-Lockout-Time at 40 dB threshold and 40 dB preamplification. The data acquisition rate of AE signals was at 10 MS/s. The storage and the loss modulus as well as glass transition temperature (T_g) of both rSCF/EP and pDop-rSCF/EP composites were characterized by dynamic mechanical analysis (DMA, Q800, TA) at a heating rate of 10 °C/min from 35 to 250 °C. In-plane

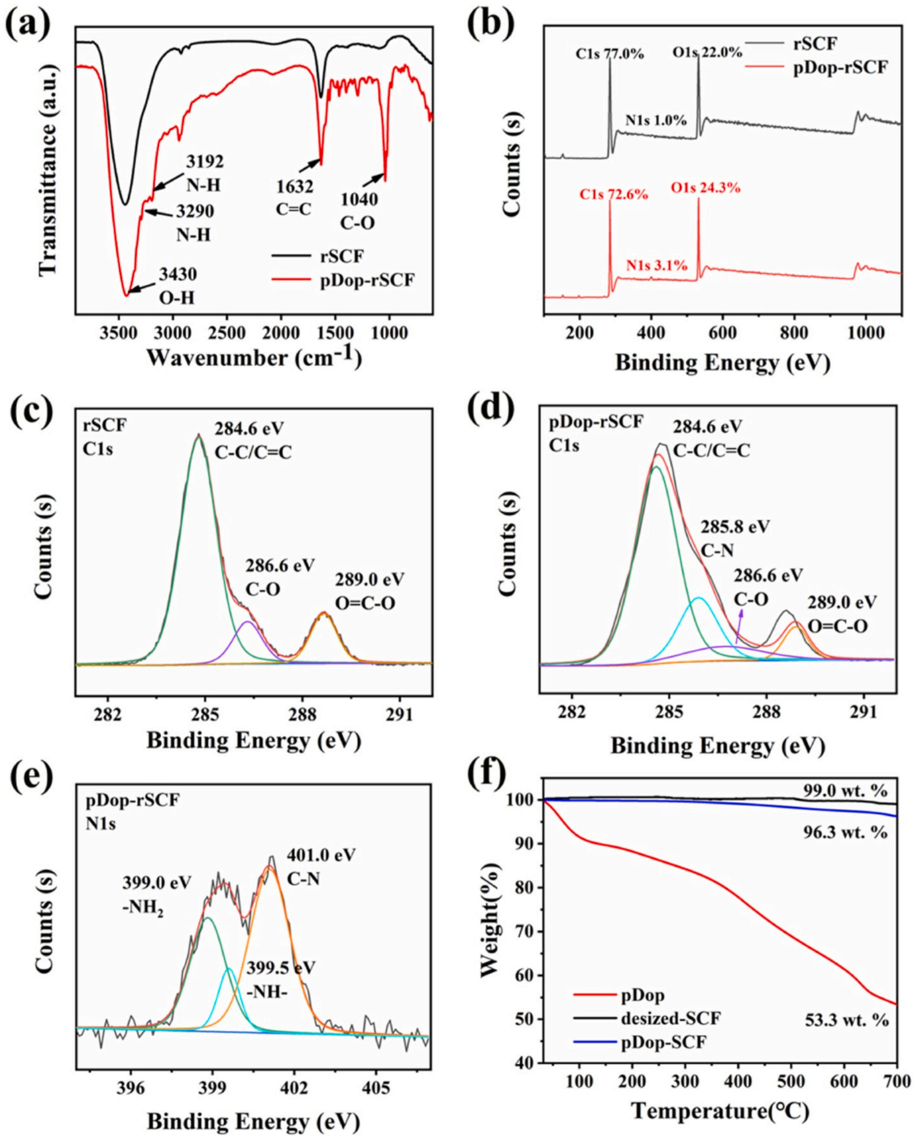

Fig. 2. (a) FTIR spectra and (b) survey XPS spectra of rSCF and pDop-rSCF, (c) C1s for rSCF, (d) C1s and (e) N1s for pDop-rSCF, as well as (f) TGA curves of rSCF and pDop-rSCF under nitrogen atmosphere.

electrical conductivity was measured on rectangular samples with dimensions of 16 × 16 × 2 mm by conductivity meter (34420A, Agilent). All final values of electrical properties were averages of five measurements. The electromagnetic shielding effectiveness (EMI SE) test was performed by Network Analyzer (Agilent N5234A) equipped with an amplifier and a scattering parameter (S-parameter) test set at the frequency range of X-band (8.2–12.4 GHz). Rectangular samples with dimensions of 23 × 10 × 2 mm were fixed into the waveguide sample holder.

3. Results and discussion

3.1. Characterization of pDop-rSCF

Identification of polydopamine on the surface of pDop-rSCF was performed by FTIR, XPS and TGA. As shown in the FTIR spectra (Fig. 2a), the characteristic aromatic C═C stretching band of rSCF was clearly observed at 1632 cm^{-1}. For the FTIR spectrum of pDop-rSCF, the additional peaks appeared at 3192 and 3290 cm^{-1}, which were originated from the N–H stretching vibration in polydopamine. And pDop-rSCF exhibited a new distinct peak at 1040 cm^{-1}, which corresponded to the shearing vibration of C–O groups connecting with aromatic rings in polydopamine. Then, surface compositions of pDop-rSCF were identified by XPS analysis (Fig. 2b–e). In Fig. 2b, both rSCF and pDop-rSCF displayed C_{1s} signal at 284.6 eV and O_{1s} signal at 533.2 eV, which were assigned to the graphitic carbons and oxygen-containing groups, respectively. In addition to the above two signals, an obvious N_{1s} signal at 401.0 eV was observed in pDop-rSCF, which was definitely attributed to the nitrogen atom in polydopamine. Deconvolution of the C_{1s} peak in the XPS profile of rSCF demonstrated three signals at 289.0, 286.6 and 284.6 eV, corresponding to O═C–O, C–O and C–C/C═C, accordingly (Fig. 2c). While in the case of pDop-rSCF, a new C–N component at 285.5 eV was identified by deconvolution of the C_{1s} peak, which was attributed to C–N structure in polydopamine (Fig. 2d). In Fig. 2e, the N_{1s} peaks of pDop-rSCF appearing at 401.0, 399.5 and 399.0 eV were originated from the C–N, –NH– and $–NH_2$ structure, respectively, which were highly consistent with the polymerization mechanism of dopamine proposed by Hong S et al. [40]. Besides, the relative atomic content proportion of C/N/O changed from 77.0/1.0/22.0 to 72.6/3.1/24.3 after polydopamine modification. The C/O atomic ratio was calculated to be 3.5 for pDop-rSCF, which was lower than the value 3.9 for rSCF. All the above facts clearly confirmed the successful modification of polydopamine onto the surface of rSCF. TGA analysis was used to determine the weight fraction of polydopamine on the surface of rSCF. In the case of polydopamine, the main decomposition occurred at the temperature above 200 °C, which was attributed to the quick loss of active groups like –OH and $–NH_2$ containing in polydopamine. rSCF showed good thermal stability with almost no weight loss as shown in Fig. 2f, due to its super-high carbon structure quantity. In contrast, pDop-rSCF started to lose weight at around 200 °C, which was in good agreement with the decomposition temperature of polydopamine. The weight fraction of polydopamine on the surface of pDop-rSCF could be calculated by following formula:

$$Xf_{pDop} + (1-X)f_{rSCF} = f_{pDop-rSCF} \tag{9}$$

where $f_{pDop}, f_{rSCF}, f_{pDop-rSCF}$ are the weight loss fraction of polydopamine,

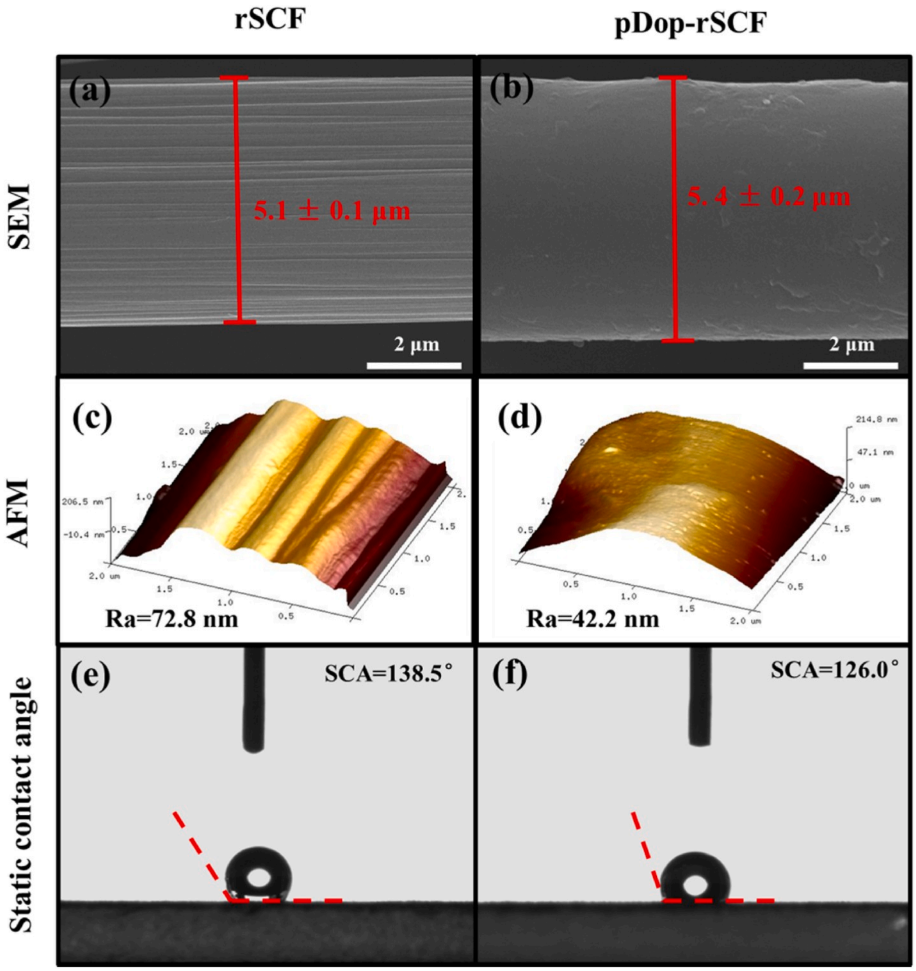

Fig. 3. (a, b) SEM, (c, d) AFM and (e, f) static contact angle images of (Left column) rSCF and (Right column) pDop-rSCF.

rSCF and pDop-rSCF at 700 °C, accordingly, and *X* denotes the weight fraction of polydopamine in pDop-rSCF. The calculated weight fraction of polydopamine in pDop-rSCF were 5.9 wt%.

The morphological state of pDop-rSCF was then evaluated with characterizations of SEM, AFM and static contact angle (Fig. 3). It could be observed from SEM images that rSCF showed a rough surface with the inherited morphology of distinct longitudinal grooves (Fig. 3a), while these grooves were almost completely filled in the case of pDop-rSCF, having a much smoother surface (Fig. 3b). And the average diameter of pDop-rSCF slightly increased to 5.4 ± 0.2 μm from 5.1 ± 0.1 μm of rSCF. The surface roughness difference between rSCF and pDop-rSCF was further confirmed and quantitatively measured using AFM. Similar to SEM images, pDop-rSCF demonstrated a much smoother and flatter surface than rSCF. After the surface modification on rSCF using polydopamine, the Ra value was reduced from 72.8 to 42.2 nm (Fig. 3c and d). These typical SEM and AFM images identified the presence of polydopamine on the surface of rSCF with uniform distribution. Moreover, the presence of polydopamine changed the surface wettability characteristics of rSCF. The static contact angle in water was tested to be 126.0° for pDop-rSCF, which was smaller than the 138.5° for rSCF (Fig. 3e and f). Also, the dynamic contact angle on pDop-rSCF showed the decreasing tendency to be 69.2° in water, compared with the value 83.7° on rSCF (Table 1). Besides, as shown in Table 1, the total surface energy on pDop-rSCF was 39.1 mN/m, being higher than 32.4 mN/m on rSCF. This enhancement in total surface energy on pDop-rSCF was mainly dependent on the contribution from obvious increasing of polar component (γ_f^p), which resulted from active functional groups (such as amine groups and phenolic hydroxyl groups) containing in polydopamine coating. Actually, the dispersive component (γ_f^d) of surface energy on pDop-rSCF decreased, indicating the decreasing in the roughness on pDop-rSCF. In summary, polydopamine-based surface modification significantly enhanced surface hydrophilicity of rSCF by introducing active functional groups, which would definitely contribute to achieving the uniform dispersion of pDop-rSCF in water-based suspension.

3.2. *Evaluation on dispersion state of pDop-rSCF*

For preparing the high quality nonwoven mat and composites using pDop-rSCF, it was necessary to evaluate its dispersion state in water. To achieve this goal, the effect of the concentration of pDop-rSCF on its dispersion state was investigated by introducing crowding factor N and dispersion coefficient β. Both values of N and β could reflect the level of inter-fiber contact in a fiber suspension as well as the tendency to form aggregates. The lower value of N or the higher value of β, the better dispersion state of pDop-rSCF would be achieved. Normally, when $N < 1$, fibers were free to move relative to one another, indicating the excellent dispersion in the suspension. As denoted in the insets of Fig. 4a, the critical concentration of fibers for ideal dispersion could be determined at $N = 1$. As N increased to a higher value (such as 16 as found in this study), fibers were gradually connected and more collisions took place. Specifically, in the case that the value of N reached a very high level, the entanglement of fibers was rather serious to form a continuous network, resulting in poor dispersion of fibers [32,41,42]. As shown in Fig. 4a, the value of N increased and the value of β accordingly decreased with the concentration for both rSCF and pDop-rSCF suspensions. When the concentration was less than 2 g/L, both rSCF and pDop-rSCF suspensions showed relatively high values of β (>0.8) and relatively low value of N (<5). When the concentration continuously increased more than 7 g/L, the value of β began to decline markedly along with the sharp increase of N to over 16, indicating that fibers were connected to form a "floppy" state. Finally, the value of β almost leveled off when N increased as high as close to 60, indicating that fibers were connected to become a rigid state. As denoted in the insets of Fig. 4a, the characteristic concentrations for connectivity threshold and rigidity threshold of both rSCF and pDop-rSCF suspensions were achieved when $N = 16$ and 60, respectively. However, the value of β was always higher for pDop-rSCF suspension than rSCF suspension at the all concentration range, which illustrated that pDop-rSCF had the better dispersion ability in water. Based on the data in Fig. 4a, the optimum dispersion concentration C_m of pDop-rSCF was determined to be 2 g/L, in which the N value was as low as 4.6, indicating the excellent dispersion state of pDop-rSCF as predicted theoretically. At this concentration condition, the differences in dispersion state of both rSCF and pDop-rSCF were further discussed in the following part of this study.

Table 1
Dynamic contact angles and surface energies for rSCF and pDop-rSCF.

Samples	θ_{water} (°)	$\theta_{\text{diiodomethane}}$ (°)	γ_f^d(mN/m)	γ_f^p(mN/m)	γ_f (mN/m)
rSCF	83.7	62.0	27.4	5.0	32.4
pDop-rSCF	69.2	63.3	26.7	12.4	39.1

Then, the dispersion states of both rSCF and pDop-rSCF in water were further compared from macroscopical and microscopical levels. Macroscopical randomness indicated the positional arrangement of the fiber groups in global scale. Fig. 4b shows fiber weight distribution and dispersion coefficient β in both suspensions with a concentration of 2 g/L. The fiber weight distribution was based on the tested results on 10 samples which were obtained by drying the specimens taken out from suspension randomly. Compared to that of rSCF suspension, the fiber weight of pDop-rSCF suspension was distributed in a narrow value range. Thus, the value of dispersion coefficient β was closer to 1 for pDop-rSCF suspension, much higher than that for rSCF suspension. This indicated the high degree macroscopical randomness of pDop-rSCF with better dispersion in water. Besides, the microscopical randomness of pDop-rSCF in the suspension was confirmed from the direct observation using OM, which implied the positional arrangement of individual fiber monofilaments in local scale. It could be seen from Fig. 5a and b that the pDop-rSCF was uniformly dispersed in water, whereas the rSCF showed local aggregates existing in the suspension. On the basis of this objective observation, the fractal dimension D was applied to detect the dispersion state of pDop-rSCF quantitatively. The obtained OM images were firstly converted to border images, which demonstrated the dispersibility of fibers and the presence of agglomerates in the suspension more clearly. More uniform the fiber distribution was, more border lines there were. Actually, the fractal dimension D was an evaluation of space filling efficiency of the aggregate structures. The fractal dimension D is applied and determined by the definition of $N(r_i) \propto \left(\frac{1}{r_i}\right)^D$, where $N(r_i)$ represents the projected area of the object (here is the border line of fibers) and r_i is the mesh size used to divide projected area of the object. Theoretically, the two-dimensional D value equaled to 2 for the case that the distribution of the object was absolutely uniform. The more deviation of the D value from 2 meant that the distribution of the object worsened more. A lower D value was corresponded to a larger area proportion of aggregates in unit area. The original data of $N(r_i)$ and r_i were directly acquired from binary images in Fig. 5c and d using software ImageJ, and D values were provided as shown in Fig. 5e and f. As a result, the average value of D (<D>) for the pDop-rSCF suspension was 1.71 obviously higher than 1.57 for rSCF suspension, which was consistent with the data of dispersion coefficient β. All these evidences proved that the polydopamine-based surface modification significantly enhanced the dispersibility of rSCF in water.

The structural uniformity of the obtained rSCF and pDop-rSCF nonwoven mats were evaluated in macroscopical and microscopical scales (Fig. 6). In the digital image of rSCF mat, global aggregates could be observed as marked by red circles (Fig. 6a), while fibers in the pDop-rSCF mat showed uniform dispersion state even without small

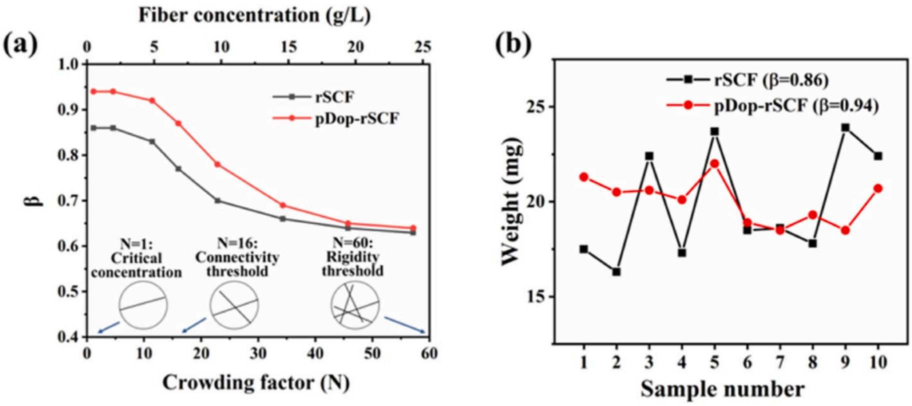

Fig. 4. (a) Effects of the concentration on the dispersion state of rSCF and pDop-rSCF in water, and (b) fiber weight distribution and dispersion coefficient β in rSCF suspension and pDop-rSCF suspension at a concentration of 2 g/L.

aggregates (Fig. 6b). SEM examination further confirmed this aggregation phenomenon in rSCF mat from the microscopical scale. rSCF tended to exist in form of bundles due to the strong friction between rSCFs and the poor surface wettability of rSCF (Fig. 6c). In contrast, polydopamine modification made the surface of pDop-rSCF smoother to reduce the friction, thereby no junctions between pDop-rSCFs were found in the microstructure of pDop-rSCF mat (Fig. 6d).

Therefore, the above results evoked our keen interest in studying the dispersion mechanism of pDop-rSCF under the assistance of polydopamine. The dispersion process of pDop-rSCF in water could be explained from two aspects of fluid mechanics and surface chemical affinity theory (Fig. 7). In one aspect, the fibers suspending in a fluid under shear experienced two competing types of interaction (Fig. 7a): hydrodynamic lubrication (F_l) and coulombic friction (F_f) [41,43]. The hydrodynamic lubrication (F_l) was the resultant of shear force derived from velocity gradient as well as the hydrophilicity of fibers. If the hydrodynamic lubrication (F_l) was much beyond coulombic friction (F_f), the fibers, which were rSCF or pDop-rSCF in our case, could be separated and then dispersed gradually. In the other aspect, due to the rough surface and poor surface wettability of rSCF, F_f was far higher than F_l so that rSCF was difficult to be dispersed (Fig. 7b). In contrast, the surface modification on rSCF by polydopamine made the surface of rSCF smoother in the point view of fluid mechanics, which reduced the coulombic friction (F_f) between fibers. Besides, the surface energy and hydrophilicity of rSCF were further increased after such modification, which increased hydrodynamic lubrication (F_l) and promoted water to infiltrate fibers faster. More importantly, the active functional groups (such as amine groups and phenolic hydroxyl groups) containing in polydopamine coating could form abundant hydrogen bonds with water molecule, which reduced the possibility of fiber re-aggregation greatly (Fig. 7c). As a result, the high degree dispersion of pDop-rSCF in water as well as the fine structural uniformity of pDop-rSCF nonwoven mat, especially in microscopical scale, was achieved in comparison with rSCF.

3.3. Performance of pDop-rSCF/EP composites

With the aim of evaluating the effect of surface chemical modification strategy on rSCF in the application of composites, pDop-rSCF was applied to prepare EP-based composites using pDop-rSCF nonwoven mat as the reinforcement. The mechanical and electrical properties of the resulted composites were measured using rSCF nonwoven mat reinforced samples as comparisons. Fig. 8a and b showed tensile and flexural properties of pristine EP and EP composites with 30 wt% rSCF mat or 30 wt% pDop-rSCF mats. In comparison with the data of pristine EP, both composites with rSCF and pDop-rSCF demonstrated much higher tensile and flexural properties, showing the typically reinforcing effect of fibers. The tensile strength and modulus of rSCF/EP composites reached 120.5 ± 18.5 MPa and 19.8 ± 1.8 GPa respectively. In contrast, these two values increased up to 147.9 ± 8.8 MPa and 22.5 ± 1.0 GPa, respectively, for pDop-rSCF/EP composites (Fig. 8a). Similar trend was detected in flexural properties of composites. Specifically, the flexural strength and modulus of pDop-rSCF/EP composites were further enhanced by 35.4 and 14.2%, respectively, compared with those of rSCF/EP composites (Fig. 8b). These results clearly confirmed that the mechanical properties were higher for EP composites reinforced by pDop-rSCF than by rSCF. Noticeably, pDop-rSCF/EP composites showed a narrow standard deviation range in the measured mechanical values than rSCF/EP composites did. The observed significant increase in mechanical properties of pDop-rSCF/EP composites was resulted from two sides. Firstly, the uniform micro-structure of pDop-rSCF nonwoven mat reduced the stress concentration and defects, which thus contributed to enhancing the mechanical properties of composites and ensuring the stability in related mechanical performance. Secondly, the surface chemical modification on rSCF by polydopamine strengthened the interfacial bonding between pDop-rSCF and EP matrix, promoting stress transfer from EP matrix to pDop-rSCF in the composites. More importantly, the strong interfacial bonding and uniform dispersion enriched the interfacial contact area between pDop-rSCF and EP matrix, which definitely guaranteed the effective filling fraction of pDop-rSCF and exerted the reinforcing effect of pDop-rSCF on the composites.

AE registration was used to study the damage development by recording sound waves originated inside composites when strain energy was released due to the formation and propagation of various types of microcracks [38,44–47]. The representative stress-strain curves with cumulative AE energy of both rSCF/EP and pDop-rSCF/EP composites under tensile loads were measured as shown in Fig. 8c and d. In the case of rSCF/EP composites, the stress-strain curve showed the typical shape for brittle damage. The cumulative AE energy manifested the steady increase and spiked at the moment of specimen fracture, indicating that the damage mechanism was dominated by matrix cracking with relatively low AE energy releasing. In the case of pDop-rSCF/EP composites, the stress-strain curve also showed the feature for brittle damage, but with higher stress at the fracture point. The values of cumulative AE energy were 139 and 943 pJ before and after fracture, respectively, which were much higher than those (39 and 565 pJ) for rSCF/EP composites. It needed to be emphasized that several sharp jumps were observed in the cumulative AE energy curve of pDop-rSCF/EP composites, however, which was not found in the case of rSCF/EP composites. In fact, each jump represented the occurrence of much more or higher acoustic energy events such as fiber breakage at a certain point. The higher cumulative AE energy along with more AE events indicated more fiber breakage in pDop-rSCF/EP composites due to the effective stress transfer between pDop-rSCF and EP matrix. In order to further analyze the damage mechanism in both rSCF/EP and pDop-rSCF/EP

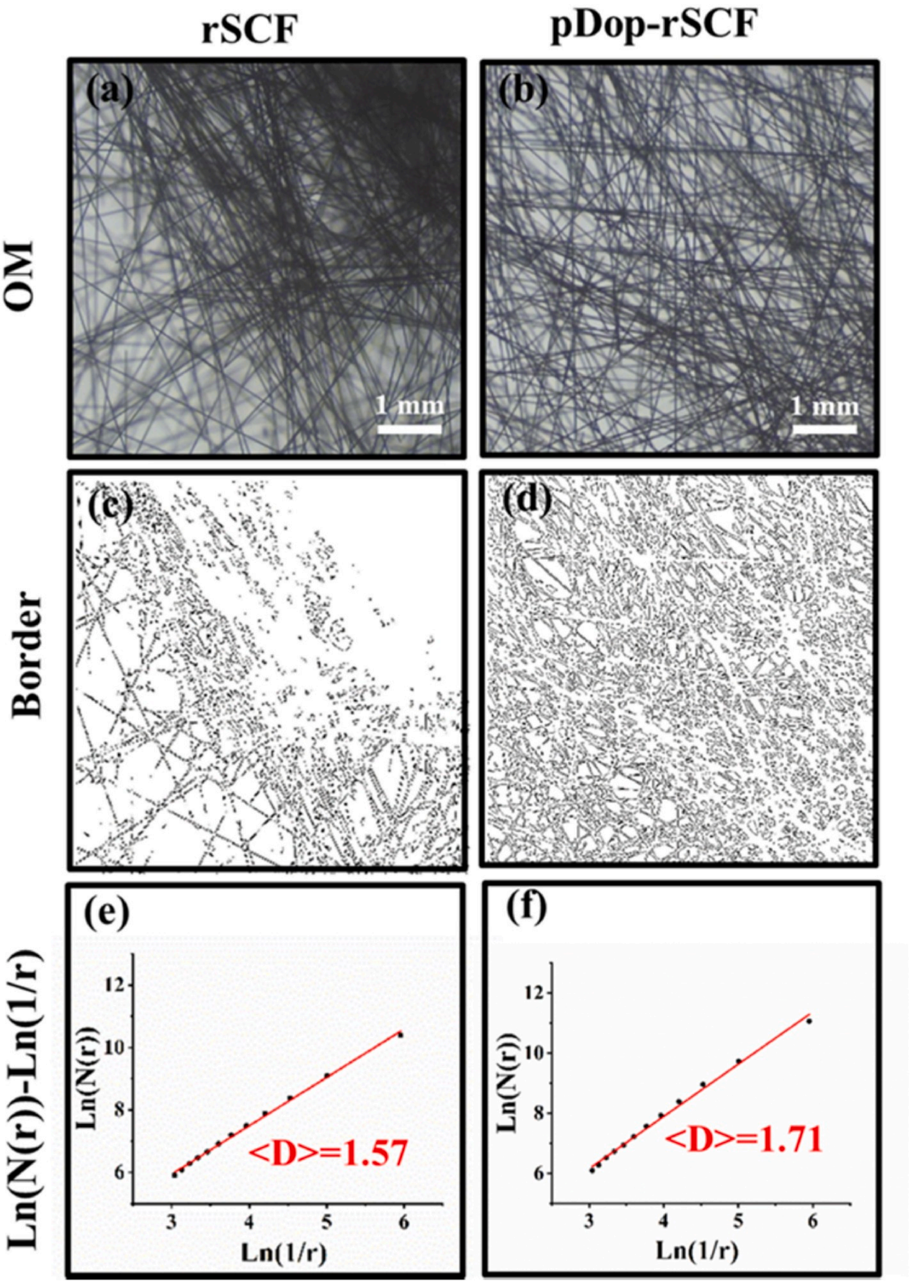

Fig. 5. (a,b) OM images, (c,d) border images and (e,f) D value linear-fit of (Left column) rSCF suspension and (Right column) pDop-rSCF suspension at a concentration of 2 g/L. In panel (e,f), the linear fit (correlation coefficient $R > 0.99$) is performed on the experimental relationship curves of $\mathrm{LnN}(r_i)$ versus $\mathrm{Ln}(\frac{1}{r_i})$, and the slopes of the curves are the two-dimensional fractal dimensions D.

composites, the obtained AE events were classified into three types (fiber breakage, interfacial failure and matrix cracking) by k-means algorithm referring to the literatures [44,46], in considering amplitude and duration time of AE events (Fig. 8e and f). It was detected that matrix cracking was the main failure mode in rSCF/EP composites, while fiber breakage rarely occurred as shown in Fig. 8e. Interestingly, the AE events caused by fiber breakage and interfacial failure occurred much more frequently in pDop-rSCF/EP composites than in rSCF/EP composites. In details, the poor interfacial debonding were very likely to happen and the debonding process was usually instantaneous in rSCF/EP composites. As a result, the poor stress transferring from matrix to fiber caused less fiber breakage. Thus, the fiber breakage and interfacial failure generated less AE events in the case of rSCF/EP composites. Differently, concerning pDop-rSCF/EP composites, the AE events induced by the fiber breakage and interfacial failure were more frequent because the stronger interfacial bonding led to the processive microcracking propagation at the interfacial region when the stress was effectively transferred from matrix to fiber. Besides, as the strain increased, all three types of AE events happened more frequently in pDop-rSCF/EP composites than in rSCF/EP composites. All these evidences stated that stress were well transferred in pDop-rSCF/EP composite, due to the uniform dispersion of pDop-rSCF and the strengthened interfacial bonding between pDop-rSCF and EP matrix. The testing of ILSS was an effective method to evaluate the interfacial bonding between fibers and matrix [4,48,49]. As shown in Table 2, the ILSS value was as high as 20.0 ± 0.6 MPa with smaller standard deviation for pDop-rSCF/EP composites, showing a 27.3% increment over that of rSCF/EP composites. This clearly verified the positive effect of polydopamine on interfacial bonding between fibers and EP matrix.

pDop-rSCF had demonstrated effective reinforcing effect on EP

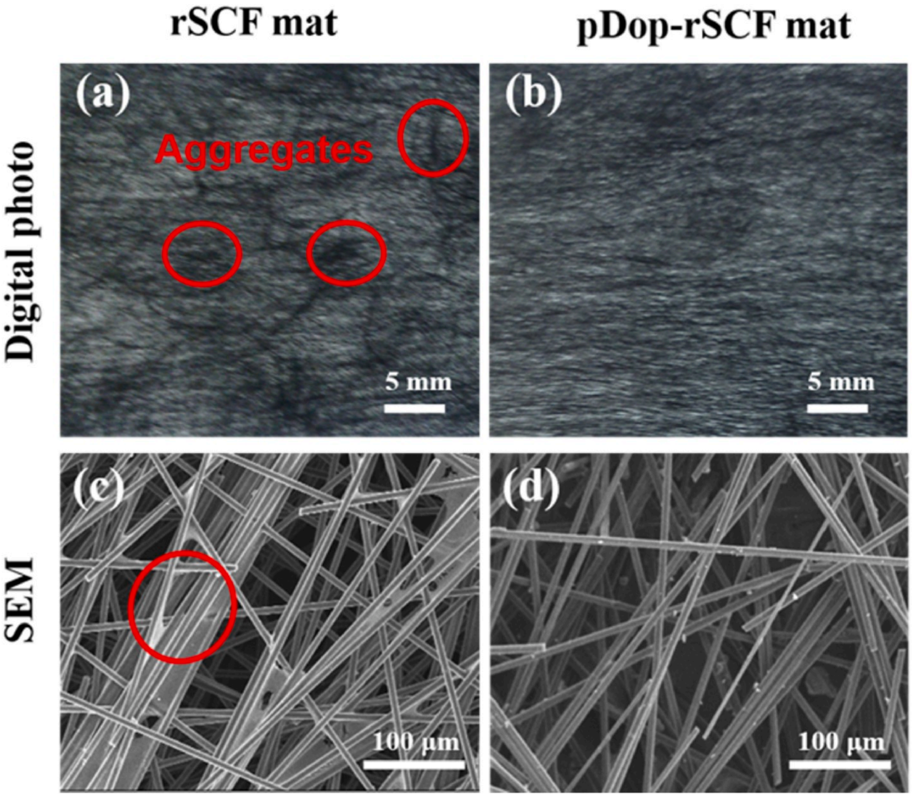

Fig. 6. (a, b) Digital and (c, d) SEM images of (Left column) rSCF and (Right column) pDop-rSCF nonwoven mats. The fiber aggregates were marked in red circles. (For interpretation of the references to colour in this figure legend, the reader is referred to the Web version of this article.)

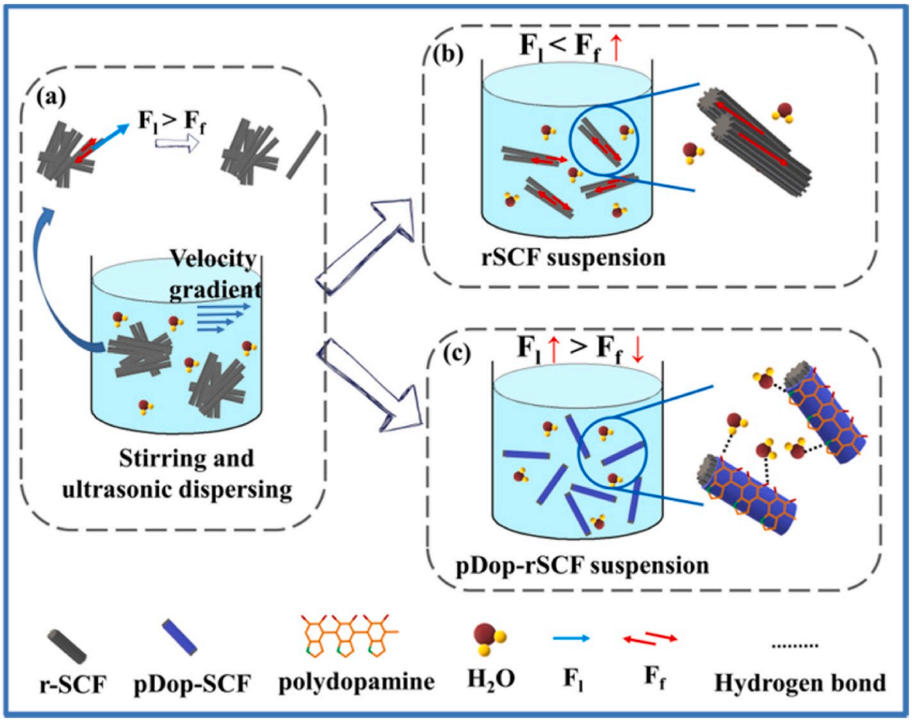

Fig. 7. Schematic diagram showing (a) dispersion process and (b,c) dispersion mechanism of (Upper right) rSCF and (Lower right) pDop-rSCF in water-based suspension.

composites by combining the inherent adhesive feature of dopamine and the interfacial amine-EP reaction. As shown in Fig. 9a, there was no chemical reaction possibility at the interfacial area in rSCF/EP composites. Differently, the primary and secondary amine groups on pDop-rSCF could be reactive with epoxide group of EP matrix. pDop-rSCF showed the capacity to enhance the curing process of EP resin. The reactions between pDop-rSCF and EP resin enabled pDop-rSCF being involved into the crosslinked structure of EP matrix during thermal

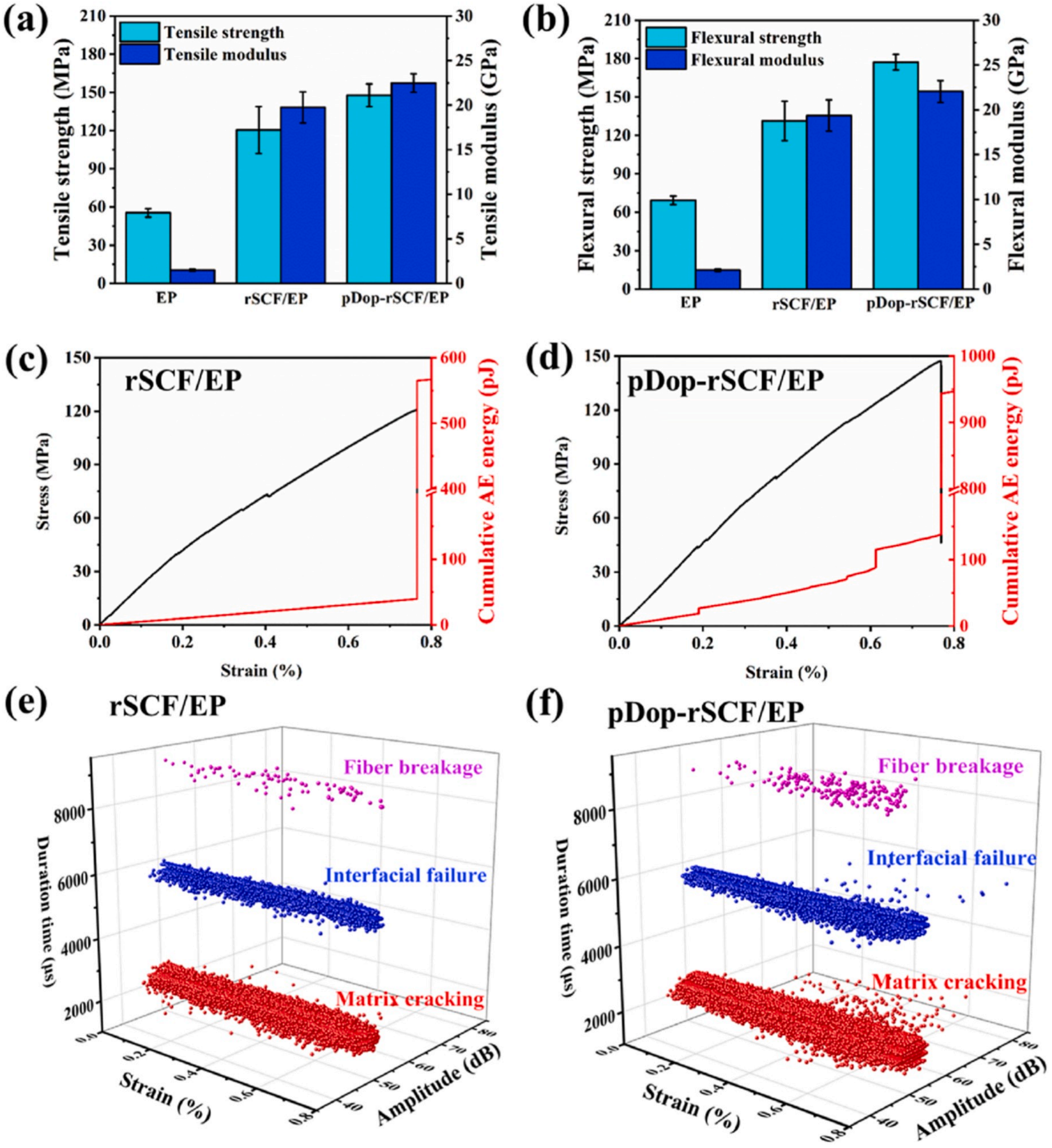

Fig. 8. (a) Tensile and (b) flexural properties of pristine EP, rSCF/EP composites and pDop-rSCF/EP composites, and representative stress-strain curves with cumulative AE energy of (c) rSCF/EP composites and (d) pDop-rSCF/EP composites under tensile loads, as well as the amplitude and duration time vs. strain of (e) rSCF/EP composites and (f) pDop-rSCF/EP composites for different damage mechanisms.

Table 2
ILSS and in-plane electrical conductivities of rSCF/EP and pDop-rSCF/EP composites.

Samples	ILSS (±std. dev.) (MPa)	In-plane electrical conductivity (S/m)
rSCF/EP	15.7 ± 1.4	20.6
pDop-rSCF/EP	20.0 ± 0.6	22.4

curing, which led to a strong interfacial bonding (Fig. 9b and c). The testing of DMTA was used to further confirm the chemical affinity between pDop-rSCF and EP matrix, together with rSCF/EP as reference (Fig. 10). The values of complex modulus E* (storage modulus E′ and loss modulus E”) and the glass transition temperature (T_g) were key parameters in relation to composite stiffness and chain movement. Storage modulus (E′) represented the elastic portion of a viscous elastic material, which reflected the performance of materials such as stiffness, degree of crosslinking, filler/matrix interfacial bonding. Stiffer the composite was, higher the E′ value would be resulted [50]. Loss modulus (E″) represented the viscous behavior and dissipated energy of the material during the stress cycle [51]. It was found that pDop-rSCF/EP composites displayed higher E’ value and E” peak value than rSCF/EP composites, exhibiting the obvious stiff and damping characteristics. The damping characteristics indicated that the strengthened interfacial bonding enhanced the dissipation energy by increasing the internal friction in pDop-rSCF/EP composites. Similarly, harder the movement of polymer chain was, higher T_g would be detected. It was observed from Fig. 10c that pDop-rSCF/EP composites displayed higher T_g value than rSCF/EP composites.

The cole-cole plot was a valuable analysis to provide more infor-

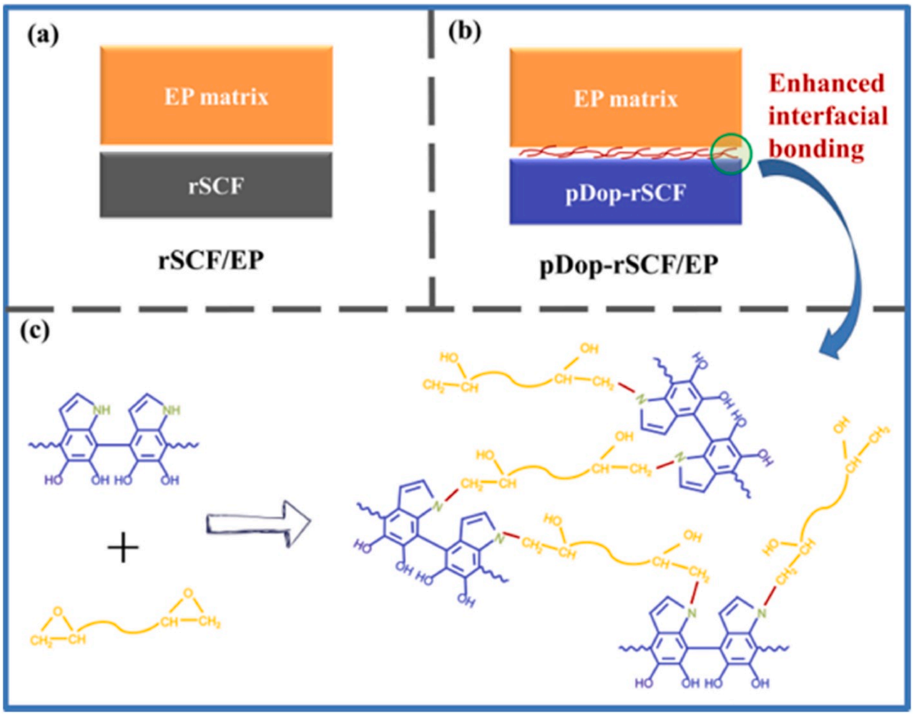

Fig. 9. Schematic diagram showing interfacial bonding of (a) rSCF/EP and (b) pDop-rSCF/EP composites, and (c) reaction mechanism between polydopamine on pDop-rSCF and EP matrix at the interfacial area. The graph in panel (c) was the high magnification of the interfacial area in pDop-rSCF/EP composites as circled area in panel (b).

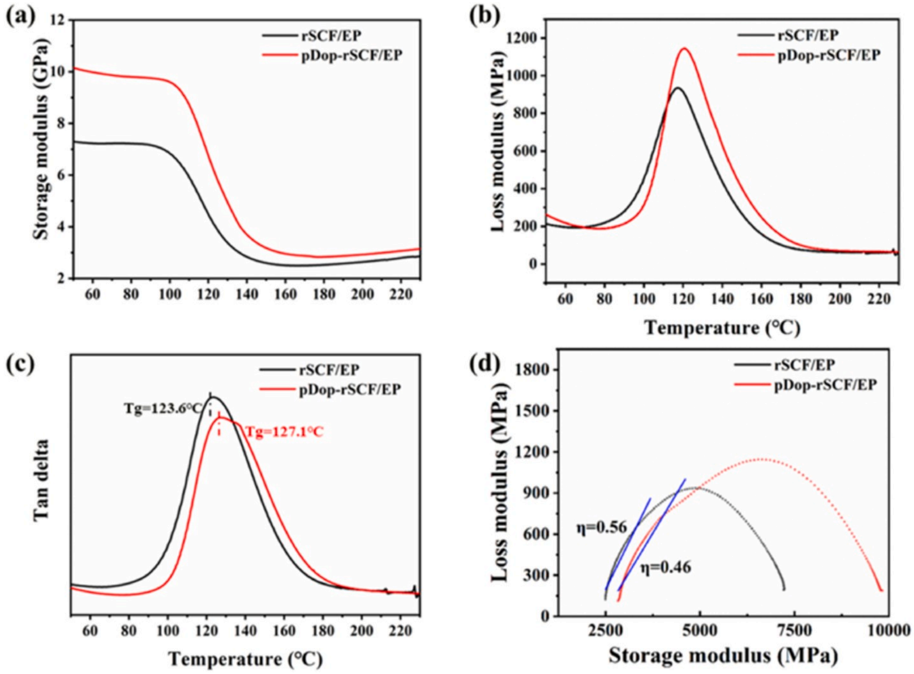

Fig. 10. (a) Storage modulus (E′), (b) loss modulus (E″), (c) tan δ vs temperature curves and (d) cole-cole plots of rSCF/EP and pDop-rSCF/EP composites.

mation on the interfacial bonding in polymer-based composites. Gerard et al. used the cole-cole approach and proposed a limited biparabolic rheological model that gave the complex modulus to describe the rheological behavior of composites, accordingly to revel the changes in EP network structure and interfacial bonding between fiber and EP [52]. Thus, the complex modulus could be written as Equation (10):

$$E^{*} = E_0 + \frac{E_\infty - E_0}{1 + (i\omega\tau_1)^{-h} + (i\omega\tau_2)^{-k}} \tag{10}$$

where ω is the pulsation, τ_1 and τ_2 are relaxation times, h and k are two parameters corresponding to long times (low frequency, high temperature) and short times (high frequency, low temperatures), respectively, as well as E_0 and E_∞ are approximated minimum and maximum values of modulus, accordingly. Specifically, the value of *k* which was closely related to the interfacial bonding state of composites, could be obtained from the left-hand slopes of the Cole-Cole plot. Better the interfacial bonding was, lower the value of *k* was. According to the published work by Gerard et al. [52], the poor chemical affinity at interfacial area led to a blocking effect of the molecular segments involved in relaxation of EP network in CF/EP composites, which accordingly increased the value of *k*. In this circumstance, an obvious decrease in *k* from 0.56 to 0.46 (deduced from the decreases of left-hand slope η) could be observed from Fig. 10d, which indicated the reduction in the blocking of segmental motion at the interface and the resulted enhancement in interfacial bonding between pDop-rSCF and EP when polydopamine was coated onto rSCF. These facts confirmed that the incorporated pDop-rSCF could interact with EP, i.e., formation of chemical interfacial bonding, which would restrict the movement of molecular chain and reduce free volume of EP matrix. Moreover, these obvious differences in the interfacial bonding could be directly examined from fractured surfaces of both rSCF/EP and pDop-rSCF/EP composites. Apparently, for rSCF/EP composites, the fractured surfaces of rSCF were smooth without EP remnants, associated with cracks and defects. The pull-out and debonding between rSCF and EP matrix were easily seen (Fig. 11a). Differently, the seamless interface between pDop-rSCF and EP matrix was found as shown in Fig. 11b. And the pulled-out fibers were tightly wrapped with EP resin, proving the excellent interfacial bonding between pDop-rSCF and EP resin.

CFRP with good electrical conductivity has widely used in the applications such as lightning strike protection materials and electromagnetic shielding materials, etc. [53–55]. It was well known that uniform filler dispersion in composites acted as a key role to enhance the electrical conductivity. Hence, the in-plane electrical conductivity was tested to evaluate the effect of pDop-rSCF filler with uniform nonwoven mat micro-structure on the electrical performance of EP composites. The in-plane electrical conductivity of rSCF/EP composites was measured to be 20.6 S/cm, indicating the conductor role of rSCF in composites, as the pure EP was an insulating materials. As expected, the in-plane electrical conductivity of pDop-rSCF/EP composites was 22.4 S/cm with a 8.7% increment after rSCF was surface-modified by polydopamine (Table 2). Objectively judging, given that the rSCF filler content (30 wt%) was much higher than percolation threshold of electrical conductivity for CF filled materials [56], this enhancement of in-plane electrical conductivity was relatively significant. As denoted in Fig. 12b, abundant rSCF (black line) tended to aggregate in rSCF/EP composites, which reduced the number of effective electrically contact points (red points) between rSCFs. Reasonably, the pDop-rSCF (blue line) with uniform nonwoven mat micro-structure formed more effective contact points between pDop-rSCFs (Fig. 12c), which built up the electrically conductive paths in the whole volume space of composites and thus enhanced the electrical conductivity of composites.

Inspired by the observed enhancement in electrical conductivity, the EMI SE of EP composites with 30 wt% rSCF or pDop-rSCF was tested at the frequency range of 8.2–12.4 GHz (Fig. 12a). It could be seen that the total EMI SE (SET) was always higher at the whole frequency range for pDop-rSCF/EP composites than rSCF/EP composites. Especially, the SET value at 8.2 GHz was up to 27 dB for rSCF/EP composites, which were in accordance with reported values for CF/polymer composites [48, 57–59]. Interestingly, a much higher SET value around 40 dB was achieved at 8.2 GHz for pDop-rSCF/EP composites, showing the advantages of surface modification in increasing electrical conductivity and electromagnetic shielding effectiveness. Normally, the SET was mainly resulted from the cumulative contributions of the reflection loss SER and the absorption loss SEA. As shown in Fig. 12a, the contribution of SEA to SET was much larger than that of SER for both rSCF/EP and pDop-rSCF/EP composites through almost the whole frequency range, indicating that absorption loss was the primary EMI shielding mechanism in these composites. The SEA value of pDop-rSCF/EP composites was noticeably enhanced compared with that of rSCF/EP composites, whereas the changes in SER were less significant. The schematic for the enhancement mechanism in electromagnetic shielding effectiveness of pDop-rSCF/EP composites was proposed. As shown in Fig. 12c, the enhancement in SEA of pDop-rSCF/EP composites was definitely attributed to the increased connectivity between pDop-rSCFs and thereby the enhanced electrical conductivity, which relied on the uniform dispersion of fillers [60,61]. Besides, the internal multiple reflections of absorbed microwave among uniform dispersed fiber network would further contribute to the enhancement in the absorption loss of pDop-rSCF/EP composites. Additionally, as found in our previous work [28], the oxygen-containing groups on pDop-rSCF surface formed electric dipole polarization due to the different abilities of carbon and oxygen atoms in catching electrons. The additional polarization relaxation process, which was caused by the electron motion hysteresis in these dipoles under alternating electromagnetic shielding field, was beneficial to enhancing EM wave absorption. And the higher number of valence electrons in the nitrogen atom than in the carbon atom was also in favor of enhancing the absorption loss SEA, since the polarization of the nitrogen-containing groups in pDop increased the interaction of the electric dipoles inside the pDop-rSCF/EP composites.

4. Conclusions

The polydopamine surface-modified rSCF (pDop-rSCF) was successfully prepared via the mild oxidative polymerization of dopamine, which distinctively offset the chemical inertness and inferior wettability of rSCF by introducing abundant amine groups and phenolic hydroxyl groups onto rSCF. Benefiting from the enhanced hydrophilicity and the resulted excellent dispersion of pDop-rSCF in water, the pDop-rSCF nonwoven mat with high structural uniformity was readily obtained through papermaking method. Thus, taking the advantages of the chemical reactivity similar to amine-type curing agent and the uniform

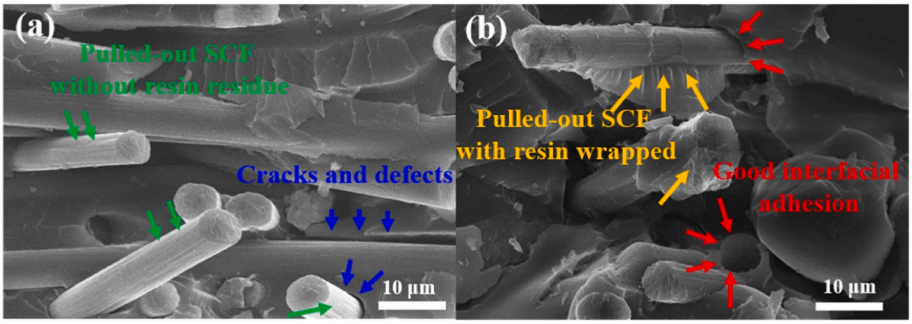

Fig. 11. SEM images of fractured surfaces in (a) rSCF/EP and (b) pDop-rSCF/EP composites. In panel (a), green arrows represent pulled-out fibers without resin remnants and blue arrows represent interfacial debonding. In panel (b), yellow arrows denote pulled-out fibers with resin remnants and red arrows denote excellent interfacial bonding. (For interpretation of the references to colour in this figure legend, the reader is referred to the Web version of this article.)

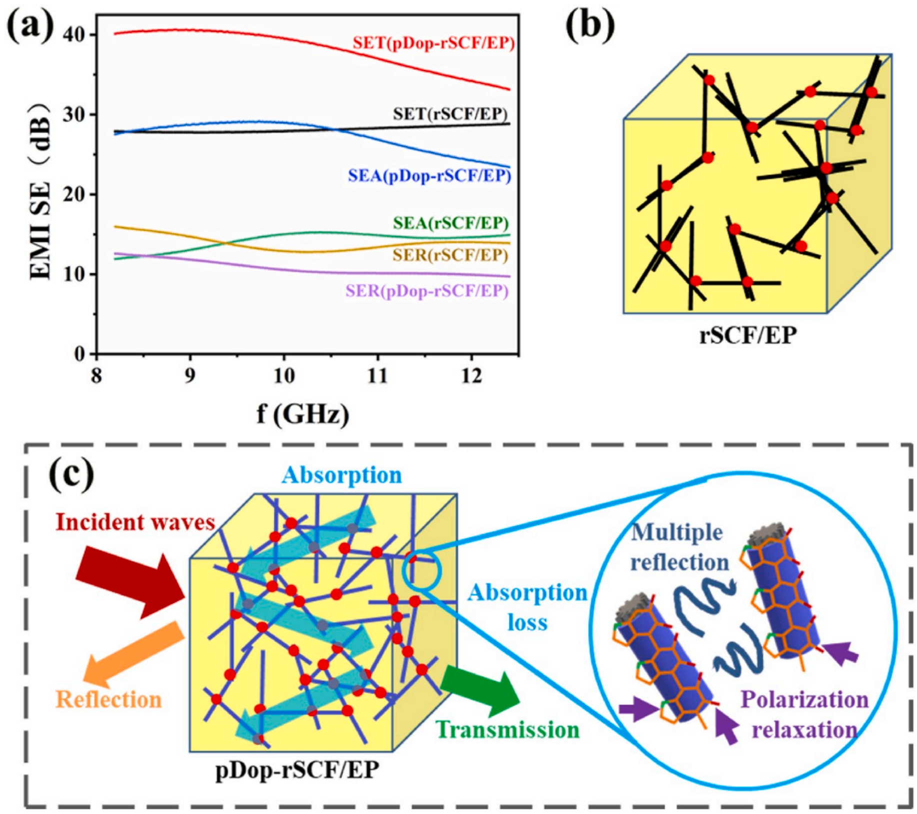

Fig. 12. (a) Electromagnetic shielding effectiveness of rSCF/EP and pDop-rSCF/EP composites, as well as sketch map of electrically conductive path in (b) rSCF/EP composites and (c) sketch map of electrically conductive path and EMI shielding mechanism in pDop-rSCF/EP composites. In panel (b) and (c), the red points represented electrically contact point between rSCFs or pDop-rSCFs. (For interpretation of the references to colour in this figure legend, the reader is referred to the Web version of this article.)

dispersion state of pDop-rSCF, mechanical properties of EP composites using pDop-rSCF nonwoven mat as reinforcement were enhanced significantly. The results of AE registration, ILSS testing and DMTA measurement identified the fact that the stress was well transferred in pDop-rSCF/EP composites due to chemically strengthened interfacial bonding between pDop-rSCF and EP matrix. Moreover, the surface modification of polydopamine onto rSCF obviously enhanced the EMI shielding property of rSCF/EP composites due to the higher electrical conductivity derived from the increased connectivity between pDop-rSCFs with uniform dispersion as well as the polarization relaxation effect induced by functional groups in polydopamine. This study provided a facile and sustainable approach to effectively reuse the rCF in polymer-based composites by synchronously promoting dispersibility and interfacial bonding of rCF in the matrix.

Declaration of competing interest

The authors declare that they have no known competing financial interests or personal relationships that could have appeared to influence the work reported in this paper.

CRediT authorship contribution statement

Xianhua Huan: Conceptualization, Methodology, Investigation, Writing - original draft. **Ke Shi:** Data curation. **Jiqiang Yan:** Validation. **Song Lin:** Writing - review & editing. **Yanjie Li:** Conceptualization. **Xiaolong Jia:** Writing - review & editing, Supervision, Project administration. **Xiaoping Yang:** Funding acquisition.

Acknowledgment

The authors are very pleased to acknowledge financial support from National Key Research and Development Project (No. 2019YFB1504800), Beijing Natural Science Foundation (Grant No. 2192044), Fundamental Research Funds for the Central Universities (Grant No. XK1802-2), National Natural Science Foundation of China (Grant No. U1362205, 5157031049, 51373016), Natural Science Foundation of Jiangsu Province (Grant No. SBK2014040489) and Beijing Youth Talent Plan (Grant No. YETP0492).

References

[1] Kwon DJ, Kim JH, Park SM, Kwon IJ, DeVries KL, Park JM. Damage sensing, mechanical and interfacial properties of resins suitable for new CFRP rope for elevator applications. Compos B Eng 2019;157:259–65.
[2] Song B, Wang T, Wang L, Liu H, Mai X, Wang X, Wang N, Huang Y, Ma Y, Lu Y, Wujcik EK, Guo Z. Interfacially reinforced carbon fiber/epoxy composite laminates via in-situ synthesized graphitic carbon nitride (g-C3N4). Compos B Eng 2019;158: 259–68.
[3] Morkavuk S, Köklü U, Bağcı M, Gemi L. Cryogenic machining of carbon fiber reinforced plastic (CFRP) composites and the effects of cryogenic treatment on tensile properties: a comparative study. Compos B Eng 2018;147:1–11.
[4] de Souza CSR, Opelt CV, Cândido GM, de Souza SDB, Botelho EC, Fernandes Marlet JM, Rezende MC. Reuse of uncured carbon fiber/epoxy resin prepreg scraps: mechanical behavior and environmental response. ACS Sustain Chem Eng 2019;7: 2200–6.
[5] Meng F, Olivetti EA, Zhao Y, Chang JC, Pickering SJ, McKechnie J. Comparing life cycle energy and global warming potential of carbon fiber composite recycling technologies and waste management options. ACS Sustain Chem Eng 2018;6: 9854–65.
[6] Longana ML, Ong N, Yu H, Potter KD. Multiple closed loop recycling of carbon fibre composites with the HiPerDiF (high performance discontinuous fibre) method. Compos Struct 2016;153:271–7.
[7] Tapper RJ, Longana ML, Hamerton I, Potter KD. A closed-loop recycling process for discontinuous carbon fibre polyamide 6 composites. Compos B Eng 2019;179: 107418.
[8] Tapper RJ, Longana ML, Yu H, Hamerton I, Potter KD. Development of a closed-loop recycling process for discontinuous carbon fibre polypropylene composites. Compos B Eng 2018;146:222–31.
[9] Pimenta S, Pinho ST. Recycling carbon fibre reinforced polymers for structural applications: technology review and market outlook. Waste Manag 2011;31: 378–92.
[10] Onwudili JA, Insura N, Williams PT. Autoclave pyrolysis of carbon reinforced composite plastic waste for carbon fibre and chemicals recovery. J Energy Inst 2013;86:227–32.

[11] Oliveux G, Dandy LO, Leeke GA. Current status of recycling of fibre reinforced polymers: review of technologies reuse and resulting properties. Prog Mater Sci 2015;72:61–99.

[12] Xu P, Li J, Ding J. Chemical recycling of carbon fibre/epoxy composites in a mixed solution of peroxide hydrogen and nn-dimethylformamide. Compos Sci Technol 2013;82:54–9.

[13] Wu TY, Zhang WY, Jin X, Liang XY, Sui G, Yang XP. Efficient reclamation of carbon fibers from epoxy composite waste through catalytic pyrolysis in molten ZnCl2. RSC Adv 2018;9:377–88.

[14] Das S, Halder S, Wang J, Goyat MS, Anil Kumar A, Fang Y. Amending the thermo-mechanical response and mechanical properties of epoxy composites with silanized chopped carbon fibers. Compos Part A: Appl S 2017;102:347–56.

[15] Lee H, Ohsawa I, Takahashi J. Effect of plasma surface treatment of recycled carbon fiber on carbon fiber-reinforced plastics (CFRP) interfacial properties. Appl Surf Sci 2015;328:241–6.

[16] Cai G, Wada M, Ohsawa I, Kitaoka S, Takahashi J. Influence of treatment with superheated steam on tensile properties of carbon fiber. Compos Part A: Appl S 2018;107:555–60.

[17] He M, Qi PF, Xu P, Cai Q, Li P, Jia XL, Yang XP. Establishing a phthalocyanine-based crosslinking interphase enhances the interfacial performances of carbon fiber/epoxy composites at elevated temperatures. Compos Sci Technol 2019;173:24–32.

[18] Sun J, Zhao F, Yao Y, Jin Z, Liu X, Huang Y. High efficient and continuous surface modification of carbon fibers with improved tensile strength and interfacial adhesion. Appl Surf Sci 2017;412:424–35.

[19] Lee H, Ohsawa I, Takahashi J. Effect of plasma surface treatment of recycled carbon fiber on carbon fiber-reinforced plastics (CFRP) interfacial properties. Appl Surf Sci 2015;328:241–6.

[20] Zhao G, Hu P, Zhou S, Chen G, An Y, Cheng Y, An J, Zhang X, Han W. Ordered silica nanoparticles grown on a three-dimensional carbon fiber architecture substrate with siliconborocarbonitride ceramic as a thermal barrier coating. ACS Appl Mater Interfaces 2016;8(6):4216–25.

[21] Wang J, Zhou S, Huang J, Zhao G, Liu Y. Interfacial modification of basalt fiber filling composites with graphene oxide and polydopamine for enhanced mechanical and tribological properties. RSC Adv 2018;8(22):12222–31.

[22] Wang P, Yang J, Liu W, Tang XZ, Zhao K, Lu X, Xu S. Tunable crack propagation behavior in carbon fiber reinforced plastic laminates with polydopamine and graphene oxide treated fibers. Mater Des 2017;113:68–75.

[23] Shanmugam L, Kazemi ME, Rao Z, Lu D, Wang X, Wang B, Yang L, Yang J. Enhanced Mode I fracture toughness of UHMWPE fabric/thermoplastic laminates with combined surface treatments of polydopamine and functionalized carbon nanotubes. Compos B Eng 2019;178:107450.

[24] Kim HJ, Song JH. Improvement in the mechanical properties of carbon and aramid composites by fiber surface modification using polydopamine. Compos B Eng 2019;160:31–6.

[25] Liu Y, Fang Y, Qian J, Liu Z, Yang B, Wang X. Bio-inspired polydopamine functionalization of carbon fiber for improving the interfacial adhesion of polypropylene composites. RSC Adv 2015;5(130):107652–61.

[26] Li WB, Shang TH, Yang WG, Yang HC, Lin S, Jia XL, Cai Q, Yang XP. Effectively exerting the reinforcement of dopamine reduced graphene oxide on epoxy-based composites via strengthened interfacial bonding. ACS Appl Mater Interfaces 2016;8:13037–50.

[27] Ma J, Pan J, Yue J, Xu Y, Bao J. High performance of poly(dopamine)-functionalized graphene oxide/poly(vinyl alcohol) nanocomposites. Appl Surf Sci 2018;427:428–36.

[28] Ren SJ, Meng L, Ma WL, Lin S, Yang WG, Lan JL, Jia XL, Cai Q, Yang XP. Enhancing overall properties of epoxy-based composites using polydopamine-coated edge-carboxylated graphene prepared via one-step high-pressure ball milling. Phys Chem Chem Phys 2019;21:21726–37.

[29] Lu L, Xing D, Xie Y, Teh KS, Zhang B, Chen S, Tang Y. Electrical conductivity investigation of a nonwoven fabric composed of carbon fibers and polypropylene/polyethylene core/sheath bicomponent fibers. Mater Des 2016;112:383–91.

[30] Liang J, Gu Y, Bai M, Wang S, Li M, Zhang Z. Electromagnetic shielding property of carbon fiber felt made of different types of short-chopped carbon fibers. Compos Part A:Appl S 2019;121:289–98.

[31] Kajiwara K, Shimoyama S, Horiguchi T US. Patent 2016;15107986:1–31.

[32] Kerekes RJ, Soszynski RM, Doo T, Punton V. Papermaking raw materials: their interaction with the production process and their effect on paper properties, vol. 2. London: Mechanical Engineering Publications Limited; 1985.

[33] Fractal dimension and lacunarity. https://imagej.nih.gov/ij/plugins/fraclac/fraclac.html. [Accessed 7 July 2019].

[34] Pérez E, Bernal C, Piacquadio M. Multifractal analysis of tensile toughness and filler dispersion for polypropylene–CaCO3 composites. Appl Surf Sci 2012;258(22):8940–5.

[35] Shi X, Pan J, Hou Q, Jin Y, Wang Z, Niu Q, Li M. Micrometer-scale fractures in coal related to coal rank based on micro-CT scanning and fractal theory. Fuel 2018;212:162–72.

[36] Liu X, Li C, Pan Y, Schubert DW, Liu C. Shear-induced rheological and electrical properties of molten poly (methyl methacrylate)/carbon black nanocomposites. Compos B Eng 2019;164:37–44.

[37] Liu X, Luo JT, Fan JF, Lin S, Jia LY, Jia XL, Cai Q, Yang XP. Comprehensive enhancement in overall properties of MWCNTs-COOH/epoxy composites by microwave: an efficient approach to strengthen interfacial bonding via localized superheating effect. Compos B Eng 2019;174:106909.

[38] Jia XL, Zhu JM, Li WB, Chen XP, Yang XP. Compressive and tensile response of CFRP cylinders induced by multi-walled carbon nanotubes. Compos Sci Technol 2015;110:35–44.

[39] Lin S, Jia XL, Sun HJ, Sun HW, Hui D, Yang XP. Thermo-mechanical properties of filament wound CFRP vessel under hydraulic and atmospheric fatigue cycling. Compos B Eng 2013;46:227–33.

[40] Hong S, Na YS, Choi S, Song IT, Kim WY, Lee H. Non-covalent self-assembly and covalent polymerization co-contribute to polydopamine formation. Adv Funct Mater 2012;22:4711–7.

[41] Li CD, Chen ZF. Effect of beating revolution on dispersion of flame attenuated glass wool suspension and tensile strength of associated glass fiber wet-laid mat. Powder Technol 2015;279:221–7.

[42] Geng L, Mittal N, Zhan C, Ansari F, Sharma PR, Peng X, Hsiao BS, Söderberg LD. Understanding the mechanistic behavior of highly charged cellulose nanofibers in aqueous systems. Macromolecules 2018;51:1498–506.

[43] Liu Y, Sun B, Li J, Cheng D, An X, Yang B, He Z, Lutes R, Khan A, Ni Y. Aqueous dispersion of carbon fibers and expanded graphite stabilized from the addition of cellulose nanocrystals to produce highly conductive cellulose composites. ACS Sustain Chem Eng 2018;6:3291–8.

[44] Kempf M, Skrabala O, Altstädt V. Acoustic emission analysis for characterisation of damage mechanisms in fibre reinforced thermosetting polyurethane and epoxy. Compos B Eng 2014;56:477–83.

[45] Gutkin R, Green CJ, Vangrattanachai S, Pinho ST, Robinson P, Curtis PT. On acoustic emission for failure investigation in CFRP: pattern recognition and peak frequency analyses. Mech Syst Signal Process 2011;25:1393–407.

[46] Munoz V, Valès B, Perrin M, Pastor ML, Welemane H, Cantarel A, Karama M. Damage detection in CFRP by coupling acoustic emission and infrared thermography. Compos B Eng 2016;85:68–75.

[47] Nikbakht M, Yousefi J, Hosseini-Toudeshky H, Minak G. Delamination evaluation of composite laminates with different interface fiber orientations using acoustic emission features and micro visualization. Compos B Eng 2017;113:185–96.

[48] Siddhartha, Gupta K. Mechanical and abrasive wear characterization of bidirectional and chopped e-glass fiber reinforced composite materials. Mater Des 2012;35:467–79.

[49] Kim JH, Kwon DJ, Shin PS, Beak YM, Park HS, DeVries KL, Park JM. Interfacial properties and permeability of three patterned glass fiber/epoxy composites by VARTM. Compos B Eng 2018;148:61–7.

[50] Chen S, Cao Y, Feng J. Polydopamine as an efficient and robust platform to functionalize carbon fiber for high-performance polymer composites. ACS Appl Mater Interfaces 2014;6:349–56.

[51] Chee SS, Jawaid M, Sultan MTH, Alothman OY, Abdullah LC. Thermomechanical and dynamic mechanical properties of bamboo/woven kenaf mat reinforced epoxy hybrid composites. Compos B Eng 2019;163:165–74.

[52] Gerard JF. Characterization and role of an elastomeric interphase on carbon fibers reinforcing an epoxy matrix. Polym Eng Sci 1988;28:568–77.

[53] Zhang R, Dowden A, Deng H, Baxendale M, Peijs T. Conductive network formation in the melt of carbon nanotube/thermoplastic polyurethane composite. Compos Sci Technol 2009;69:1499–504.

[54] Forintos N, Czigany T. Multifunctional application of carbon fiber reinforced polymer composites: electrical properties of the reinforcing carbon fibers–a short review. Compos B Eng 2019;162:331–43.

[55] Yao SS, Jin FL, Rhee KY, Hui D, Park SJ. Recent advances in carbon-fiber-reinforced thermoplastic composites: a review. Compos B Eng 2018;142:241–50.

[56] Pal G, Kumar S. Multiscale modeling of effective electrical conductivity of short carbon fiber-carbon nanotube-polymer matrix hybrid composites. Mater Des 2016;89:129–36.

[57] Rohini R, Bose S. Electrodeposited carbon fiber and epoxy based sandwich architectures suppress electromagnetic radiation by absorption. Compos B Eng 2019;161:578–85.

[58] Rohini R, Verma K, Bose S. Interfacial architecture constructed using functionalized MWNT resulting in enhanced EMI shielding in epoxy/carbon fiber composites. ACS Omega 2018;3:3974–82.

[59] Hu T, Wang J, Wang J, Chen R. Electromagnetic interference shielding properties of carbonyl iron powder-carbon fiber felt/epoxy resin composites with different layer angle. Mater Lett 2015;142:242–5.

[60] Chen Y, Zhang HB, Yang Y, Wang M, Cao A, Yu ZZ. High-performance epoxy nanocomposites reinforced with three-dimensional carbon nanotube sponge for electromagnetic interference shielding. Adv Funct Mater 2016;26:447–55.

[61] Liu J, Zhang HB, Sun R, Liu Y, Liu Z, Zhou A, Yu ZZ. Hydrophobic flexible and lightweight MXene foams for high-performance electromagnetic-interference shielding. Adv Mater 2017;29:1702367.